Article

Not peer-reviewed version

Tumor Microenvironment-Responsive Magnetotactic Bacteria-Based Multi-drug Delivery Platform for MRI-Visualized Tumor Photothermal–Chemodynamic Therapy

Feng Feng , Qilong Li , Xuefei Sun , Li Yao * , Xiuyu Wang *

Posted Date: 8 August 2024

doi: 10.20944/preprints202408.0458.v1

Keywords: MRI visualization; combination therapy; multi-drug delivery platform; magnetotactic bacterial; enhanced photothermal-chemodynamic therapy

Article

Tumor Microenvironment-Responsive Magnetotactic Bacteria-Based Multi-Drug Delivery Platform for MRI-Visualized Tumor Photothermal—Chemodynamic Therapy

Feng Feng [1,†], Qilong Li [2,†], Xuefei Sun [2], Li Yao [2,*] and Xiuyu Wang [1,*]

[1] Institute of Process Equipment, College of Energy Engineering, Zhejiang University, Hangzhou 310027, China
[2] Institute of Chemistry Chinese Academy of Sciences, Beijing 100190, China
* Correspondence: wangxiuyu@zju.edu.cn
† These authors contributed equally to this work.

Abstract: Cancer cells display elevated reactive oxygen species (ROS) and altered redox status, Here based on these characteristics, we develop a multi-drug delivery platform AMB@PDAP-Fe (APPF), from magnetotactic bacterium AMB-1 and realize MRI-visualized tumor microenvironment-responsive photothermal-chemodynamic therapy. The Fe^{3+} in PDAP-Fe is reduced by the GSH at tumor site and is released in the form of highly active Fe^{2+}, which catalyzes the generation of ROS through Fenton reaction and inhibits tumor growth. At the same time, the significant absorption of the mineralized magnetosomes in AMB-1 cells in the NIR region enable them to efficiently convert near-infrared light into heat energy for photothermal therapy (PTT), to which PDAP also contributes. The heat generated in the PTT process accelerates the process of Fe^{2+} release, thereby achieving an enhanced Fenton reaction in tumor microenvironment. In addition, the magnetosomes in AMB-1 are used as MRI contrast agent, and the curing process is visualized. This tumor microenvironment-responsive MTB-based multi-drug delivery platform displays a potency to combat tumor and demonstrates the utility and practicality of understanding the cooperative molecular mechanism when designing multi-drug combination therapies.

Keywords: MRI visualization; combination therapy; multi-drug delivery platform; magnetotactic bacterial; enhanced photothermal-chemodynamic therapy

1. Introduction

Elucidation of the various defects that underlie cancer has highlighted the complexity of cancer and emphasized the inadequacies of single-drug therapies [1,2]. Combining different therapeutics has been proven to be more effective than single-agent therapies. It has shifted cancer treatment from a focus on monotherapy to a multi-drug therapy, based on an active cooperation between two or more treatments, which may result in ostentatious super-additive (namely "1+1>2") therapeutic effects [3]. For example, chemotherapeutics combined with P-glycoprotein (P-gp) inhibitors, or tyrosine kinase inhibitors (TKIs) enhances cytotoxicity [4]. While different drug combinations have continuously been proven promising, their curing efficacy remains unsatisfactory, as they show little to no improvement and often produce severe side-effects [5]. This could be attributed to the negligence of the differences of each drug when studying their cooperative cytotoxicity. Different drugs have different physicochemical properties, and the differences in their physicochemical properties may lead to dissimilarities in their pharmacokinetics and tissue distribution and their individual toxicity profile might also differ in different tissues [6]. To overcome this problem and to realize the full potential of combination therapy, the research community has focused on developing

 doi:10.20944/preprints202408.0458.v1

different strategies to design and engineer drug delivery platforms (DDP) for the delivery of multiple drugs, as DDPs that are capable of precise and controlled delivery of drugs mitigate side effects and improve therapeutic efficacy, yielding effective combination therapies [7,8)]. Therefore, how to better design multi-drug delivery platforms so that different drugs can be better combined and effectively delivered to the action site at the same time are important frontiers in combined tumor therapy.

Multi-drug delivery platforms that are involved in combined therapy, such as metal oxide nanoparticles [9,10], biomimetic systems [11–13] (e.g., cell membrane-coated nanoparticles [13]), and internally or externally responsive nano-systems [14–16] (e.g., pH-responsive nanoparticles [15]), are generally passive carriers that lack self-motivation, and greatly rely on blood flow to passively reach tumor tissue; and because of the complicated extracellular microenvironment of tumor tissue, fibrosis for instance, and its high internal pressure, the accumulation of the therapeutics at the tumor site is less than 1% [17]. Compared with these manmade non-living multi-drug delivery carriers that have been developed in the last decades, Bacteria, as a self-propelled, engineerable microorganism, could be used as an active drug delivery system, considering their auto-mobility, which can help them migrate into solid tumors and accumulate in both hypoxia and nonhypoxia regions, and the presence of the multiple reactive molecules or proteins on the membrane, which allows different concept-based modifications [18].

Magnetotactic bacteria (MTB) are natural biomineralized bacteria that automatically synthesize magnetosomes. The magnetosomes within MTB are phospholipid bilayers-wrapped magnetite (Fe_3O_4) nanoparticle chains, or less commonly cinerite (Fe_3S_4) magnetic iron chains, which greatly enhanced the magnetic anisotropy of the nanoparticles, and have a magnetic moment of $6^* 10^{-15} Am^2$ [19]. The magnetosomes can quickly respond to external magnetic fields and help MTB to migrate and accumulate in deep tumor tissues [20,21]. Besides, MTB are often found living in oxic-anoxic regions, and their facultative anaerobic behavior is greatly beneficial to targeting the hypoxia regions in tumor tissues [22]. Combining their living preference in anoxic region and the magnetite properties of their magnetosome, MTB could be used as MRI-visualized multi-drug delivery platform. Therefore, compared to other non-living drug-delivering carriers, MTB is efficient automotive carrier to deliver multi-drugs based on different design concept. MTB provide several advantages over non-living carriers when used as multi-drug delivery carrier, including improved flexibility of navigating, improved ability to accumulate in both hypoxia and nonhypoxia tumor regions, and small invasiveness [23]. Furthermore, magnetosomes in MTB exhibit significant absorption in near-infrared (NIR) region and can convert the light energy into heat energy, which could finally result in thermal ablation of cancer**.** Therefore, MTB can not only be used as an efficient automotive multi-drug nanocarrier in tumor treatment, but also can function as an effective tumor killer in tumor photothermal therapy (PTT).

In this work, we designed a multifunctional multi-drug delivery platform AMB@PDAP-Fe (APPF) based on magnetotactic bacteria (AMB) for MRI-visualized tumor photo-thermotherapy (PTT) and enhanced chemodynamic therapy (CDT). Upon magnetic navigation, APPF accumulated in tumor tissues. The PDAP-Fe in the composite was reduced by glutathione (GSH) in tumor microenvironment and produced Fe^{2+}, which catalyzed the generation of reactive oxygen species (ROS) through Fenton reaction and thus induced tumor cell apoptosis. Upon NIR light irradiation, magnetosomes in magnetotactic bacteria immediately converted the light energy into heat energy and the tumor tissue in the NIR light spot was heated up. PDAP also contributed to the heat-up of the tumor tissue because of its own mild photothermal ability. The combined photothermal effect of AMB-1 and PDAP rapidly elevated the temperature at the tumor site, and caused tumor cell death. It is noteworthy that the heat generated during the synergistic PTT process accelerated the releasing of Fe^{2+} from PDAP-Fe, which enhanced the catalytic conversion of endogenous H_2O_2 into ·OH, and thus achieved synergistic photothermal-enhanced Fenton reaction-mediated cancer therapy. AMB@PDAP-Fe did not only kill cancer cells by chemotherapy but also greatly increased the sensitivity of tumor cells towards laser irradiation for enhanced PTT [24,25] to produced bimodal synergistic effects based on chemo-therapy-enhanced PTT, which displayed that rational therapeutic-

 doi:10.20944/preprints202408.0458.v1

combination based on a deep understanding of the underlying molecular mechanisms are potentially powerful in the treatment of cancer.

2. Materials and Methods

2.1. Materials

Potassium dihydrogen phosphate (KH_2PO_4); Sodium nitrate ($NaNO_3$); Succinic acid; L-Cysteine; Peptone; Yeast extract; Ethylenediaminetetraacetic acid (EDTA); Magnesium sulfate ($MgSO_4·7H_2O$); Manganese sulfate ($MnSO_4·4H_2O$); Sodium chloride (NaCl); Ferrous sulfate ($FeSO_4·7H_2O$); Cobalt(II) chloride hexahydrate ($CoCl_2·6H_2O$); Calcium chloride ($CaCl_2$); Zinc sulfate ($ZnSO_4·7H_2O$); Copper sulfate pentahydrate ($CuSO_4·5H_2O$); Potassium alum ($AlK(SO_4)_2$); Boric acid (H_3BO_3); Sodium tungstate dihydrate ($NaWO_4·2H_2O$); Sodium molybdate dihydrate ($NaMoO_4·2H_2O$); Nickel chloride hexahydrate ($NiCl_2·6H_2O$); Anhydrous sodium selenite (Na_2SeO_3); D-Tartaric acid; Succinic acid; Biotin; Folic acid; Riboflavin; Vitamin B12; Calcium pantothenate; Para-aminobenzoic acid; Thioctic acid; Nicotinic acid; Quinic acid; Agar purchased from Maclin; 2,6-Diaminopyridine; Ferric chloride hexahydrate; Dimethyl sulfoxide (DMSO); Hydrogen peroxide (H_2O_2); 3,3',5,5'-Tetramethylbenzidine (TMB) were purchased from Beijing Solarbio.

2.2. AMB-1 cultivation and characterization

AMB-1 (5 mL) in their logarithmic growth phase were cultivated in 200 mL sterilized culture medium in a 250 mL culture flask for 72 h and their growth curve was recorded. 100 μL of deionized water resuspended AMB-1 was transferred to a carbon-supported copper membrane and dried. The carbon-supported membrane was subjected to TEM (transmission electron microscope, HT7700) observation. The 72-hour cultured bacterial suspension was placed in a UV-visible spectrophotometer applied with vertical and horizontal magnetic field. The OD_{600} value of AMB-1 was measured at a wavelength of 600 nm. By changing the direction of the applied magnetic field, the OD_{600} value under the horizontal magnetic field "OD∥" and under the vertical magnetic field "OD⊥" were measured. The ratio of these two values represents the Cmag value.

2.3. Preparation of APPF based on magnetotactic bacteria

PDAP-Fe was prepared through Fe (III)-mediated 2,6-2 aminopyridine (DAP) oxidation polymerization. Briefly, 20 mM $FeCl_3·6H_2O$ was dissolved in 100 mL of deionized water. 20 mM DAP was added to the mixture, and stirred at 37°C for 24 hours for polymerization. Subsequently, the mixture was dialyzed and Fe-PDAP nanoparticle solution was obtained (dialysis membrane for 12 kDa MW). The Fe-PDAP solution was then freeze-dried and stored at 4°C. 10 mL of the AMB-1 bacterial with an OD_{600} value of 0.1 was centrifuged at 3000 rpm for 10 minutes. The precipitate was resuspended in 5 mL of deionized water and centrifuged again at 3000 rpm for 10 minutes. This process was repeated three times. The obtained AMB-1 precipitate was dispersed in 0.5 mL of deionized water, and 100 μL PDAP-Fe (1 mg/mL) was added before the volume was adjusted to 1 mL. The mixture was incubated at 28°C and shaken at 100 rpm for 20 minutes. After centrifugation at 2000 rpm for 15 minutes, the precipitate was collected and dispersed in deionized water, followed by three rounds of washing at 2000 rpm. The final suspension was resuspended in deionized water and APPF was obtained, which was then stored at 4°C.

2.4. In vitro photothermal performance testing

The samples were irradiated with 808 nm laser (1.0 W/cm^2, 300 s) in a sample cell. The temperature and photographs of the solution were recorded using a near-infrared thermal imaging camera every 30 s. To calculate the photothermal conversion efficiency (η), the TTIS suspension (100 μg/mL, 0.5 mL) was irradiated with 808 nm laser (1.0 W/cm^2) until the temperature stabilized. The photothermal performance of different concentrations of APPF was tested. The concentrations were set as follows: $1×10^9$ CFU/mL, $1.5×10^9$ CFU/mL, $2.0×10^9$ CFU/mL, and $4×10^9$ CFU/mL, with a volume

 doi:10.20944/preprints202408.0458.v1

of 0.5 mL. The effect of different laser powers (808 nm) on the photothermal performance of APPF was tested. The APPF concentration was set at 1×10^9 CFU/mL, and the laser powers used were 0.5 W/cm^2, 1.0 W/cm^2, and 1.5 W/cm^2. The laser irradiation was performed for 10 minutes. At last, the photothermal performance of different groups of materials was tested: PBS, PDAP-Fe, AMB-1, and AMB@PDAP-Fe. The laser power was set at 1.0 W/cm^2, and the laser irradiation was performed for 10 minutes.

2.5. Measurement of GSH-dependent iron release

The To measure the release of Fe^{2+} triggered by GSH in APPF, APPF (1×10^9 CFU/mL, 2 mL) was dispersed in phosphate buffer solutions with and without GSH (200 μM). The suspensions were dialyzed against buffer solution (pH 7.4, 10 mL) for 24 hours with a cutoff value of 12 kDa MW. At specific time intervals, equal aliquots of 1.0 mL dialysate were sampled and replaced with an equal volume of fresh culture medium. The released Fe^{2+} in the buffer solution was collected and mixed with a solution of bathophenanthroline (50 μL, 100 mM), which served as a Fe^{2+} probe (Bathophenanthroline reacts with Fe^{2+} to form a complex that exhibits absorbance at 512 nm). The concentration of released Fe^{2+} was measured using UV-vis absorption spectroscopy.

2.6. Intracellular reactive oxygen species (ROS) detection

The 4T1 tumor cells were seeded in a confocal microscopy culture dish and allowed to adhere overnight. Once the cell density reached confluency, the culture medium was replaced with 2 mL of medium containing the following substances: PBS+GSH (100 μM GSH), H2O2 (100×10^{-6} M), APPF (1×10^9 CFU/mL) + H2O2 (100×10^{-6} M), APPF (1×10^9 CFU/mL) + GSH (100 μM) + H_2O_2 (100×10^{-6} M). Different incubation times were set for each group (30 min, 1 h, 4 h for APPF+GSH group; 4 h for other groups). The cells were then washed three times with PBS. After incubating the samples with 20×10^{-6} M DCFH-DA for 15 min, the cells were observed under a confocal laser scanning microscope (Olympus-FV1000).

2.7. In vitro photothermal therapy

4T1 cells were seeded in a 96-well plate at a density of 2000 cells per well and incubated overnight. The culture medium was then replaced with 1 mL of medium containing APPF (1×10^9 CFU/mL), and the cells were irradiated with 808 nm laser (1.0 W/cm^2) for 10 minutes. After that, the cells were washed and incubated with fresh medium for an additional 12 hours, and cell viability was measured using the CCK-8 kit (Beijing Solarbio).

2.8. MRI measurement

MRI (0.5T) was used to determined T_1 and T_2 relaxation times of APPF; For T_1, Parameters were listed: repetition time (TR) =6000ms, number of data =25, and number of averages (NA) = 2; for T_2 parameters were as follow, TR = 6000ms, echo time (TE) = 1ms, echo count =6000 and NA = 2. r_1 and r_2 relaxivities were calculated using the linear fitting of $1/T_1$ or $1/T_2$ as a function of metal (Fe + Mn) concentration. For T_1- and T_2-weighted MR images, the instrument parameters were set as follows: TR = 100ms, TE = 18.2ms, imaging matrix =192 × 256, slice thickness = 5 mm, field of view (FOV) = 100 mm ×100 mm and NA = 2. In in vivo MR imaging experiments, tumor-bearing mice were anesthetized with 100μL of 10% chloral hydrate through intraperitoneal injection. 200μLAPPF solution was injected intravenously into the mouse. MR images were acquired before injection and 1, 5, and 9 h post-injection, respectively.

 doi:10.20944/preprints202408.0458.v1

2.9. In vivo anti-tumor experiment

A volume of 100 μL of 4T1 cell suspension (approximately 4×10^5 cells) were subcutaneously injected into the right hind back of 6-week-old BALB/c mice (purchased from Beijing Vital River). Tumor treatment experiments were performed when the tumors reached a volume of approximately 70-100 mm^3, typically 5-7 days following cell injection. When the tumor volume reached approximately 100 mm3, the mice were injected with 25 μL of saline solution, AMB-1 (2×10^9 CFU/mL), PDAP-Fe (72.68 μg/mL), or APPF (2×10^9 CFU/mL) around the tumor. Two hours after injection, the groups injected with saline, AMB-1, and APPF were subjected to 808 nm laser irradiation at a power density of 1.0 W/cm^2 for 10 minutes. The temperature was recorded using a thermal imaging camera. During the treatment period, the body weight and tumor size of the mice were measured daily. The tumor volume was calculated as $V=\pi/6\times L\times W^2$, where V is the tumor volume, L is the tumor length, W is the tumor width. On the 21st day, the mice were anesthetized, and 500 μL of blood was collected from each mouse. The blood was centrifuged at 2000g for 15 minutes (4°C) to obtain plasma for biochemical analysis. The mouse tumor tissue was also collected and weighed.

2.10. Statistical Analysis

All statistical analysis in this research was conducted using student's t-test through GraphPad Prism 8. (*), (**), and (***) represent $p<0.05$, $p<0.01$, and $p<0.001$, respectively. $p<0.05$ was considered significant. All data were ex-pressed as the mean with standard deviation (mean ± SD).

2.11. Ethics

All animal procedures were performed in accordance with the guidelines for the Care and Use of Laboratory Animals of Peking University Health Science Center and approved by the Animal Ethics Committee of Peking University. The assigned approval/accreditation number is LA2019083.

3. Results

3.1. Preparation and characterization of APPF

To The preparation of APPF was illustrated in Figure 1a. Fe-ion-doped PDAP-Fe was synthesized in aqueous solution using $FeCl_3$ as oxidant and 2,6-diaminopyridine (DAP) as precursor [26,27]. Subsequently, purified AMB-1 was co-incubated with PDAP-Fe. PDAP-Fe rapidly absorbed onto AMB-1 (electrostatic interaction), yielding a multifunctional platform, APPF. Transmission electron microscopy (TEM) images showed that the synthesized PDAP-Fe exhibited shuttle-like structures of approximately 40 nm (Figure 1b). The as-formed APPF retained the morphology of AMB-1, and PDAP-Fe coated AMB-1 evenly (Figure 1c). The volume of APPF was slightly larger than that of AMB-1 because of the coating. No disruption of the membrane structure of AMB-1 was observed in the magnified images (Figure 1d and e). Because PDAP-Fe was the product of Fe ions-driven DAP polymerization and Fe ions was key to the production of APPF, we analyzed the distribution of Fe elements in APPF using dark-field TEM and surface elemental mapping (Figure 1f-i). The results demonstrated a significant distribution of Fe elements on the surface of APPF, mainly in the PDAP-Fe-formed nanocoating and the magnetosomes of bacteria. The abundant loading of Fe ions provided a foundation for the efficient catalytic activity of CDT in APPF [28]. To study whether the interaction between PDAP-Fe and AMB-1 was electrostatic interaction, we analyzed their zeta potentials. AMB-1 displayed a mild negative charge before co-incubation, approximately -16.9 mV, while PDAP-Fe exhibited a positive charge, around 35.4 mV, due to the presence of amino groups in its structure. The zeta potential of APPF dropped to -3.2 mV, indicating that AMB-1 and PDAP-Fe neutralized each other and the adsorption of PDAP-Fe on AMB-1 was indeed electrostatic absorption (Figure 1j).

To study their light absorption properties, we conducted UV-visible absorption spectroscopy. APPF showed a broad absorption in the range of 300-900 nm, with a characteristic absorption peak

 doi:10.20944/preprints202408.0458.v1

of PDAP-Fe appearing at 335 nm (Figure 1k), further indicating the effective loading of PDAP-Fe in APPF. Both AMB-1 and APPF exhibited noticeable absorption in the near-infrared wavelength range (Figure 1l), implying a possibility of them being used as photothermal agents. Subsequently, we characterized the magnetic properties of APPF before and after preparation (Figure 1m). The results showed that both AMB-1 and APPF exhibited superparamagnetic behavior, and due to the presence of magnetosomes, they displayed a certain amount of residual magnetization at low fields, which was consistent with previous reports [29].

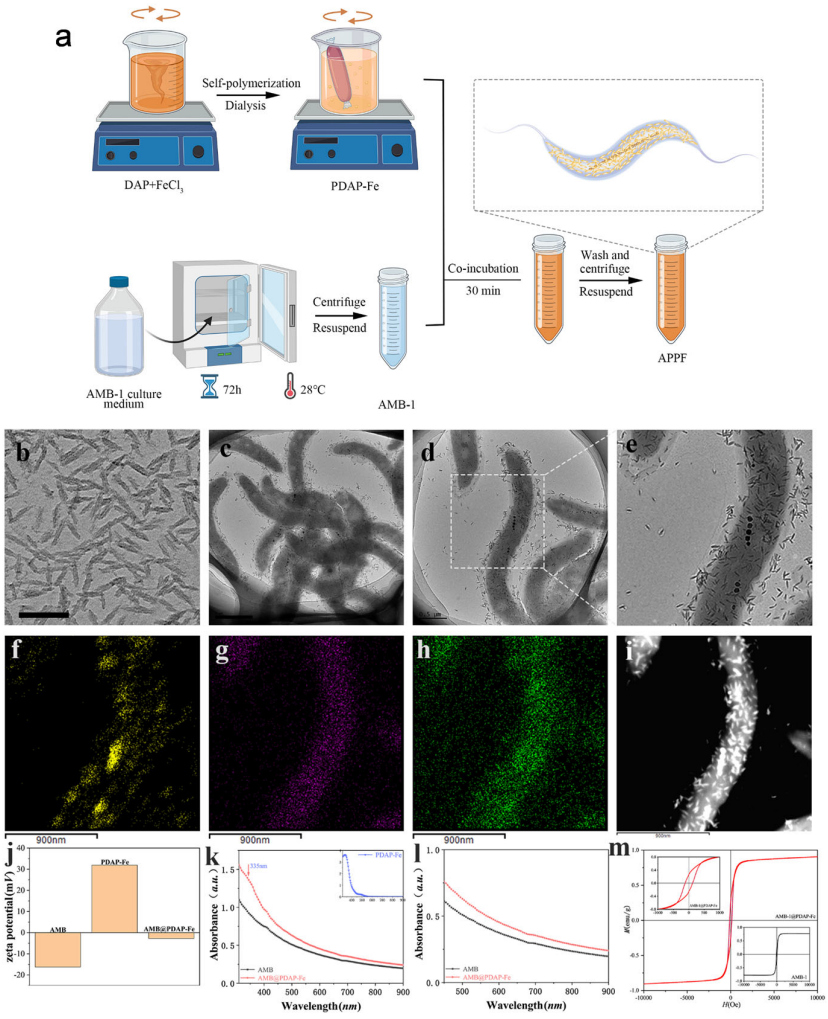

Figure 1. Preparation and characterization of APPF**.** (a) Schematic illustration of APPF preparation; (b) TEM image of PDAP-Fe, (c-e) APPF; (f-i) Elemental mapping of APPF: f) Fe, g) N, h) O and the corresponding dark-field TEM images; (j) Zeta potential of AMB-1, PDAP-Fe and APPF; (k) UV visible absorption spectra of AMB-1, PDAP-Fe and APPF; (I) Absorption spectra of AMB-1 and APPF in the infrared region; (m) M-H curves of AMB-1 and APPF at room temperature. The scale bar is 50 nm.

3.2. APPF demonstrates good photothermal effect and induces Fenton reaction in vitro

The high absorption of APPF in the NIR region enabled us to investigate its photothermal performance, which is typical for PTT applications. As shown in Figure 2a, the PBS group exhibited almost no change in temperature (1.6℃ increase within 10 min of irradiation); the PDAP-Fe group at equimolar concentration showed mild photothermal effect (5℃ increase), which failed to reach the therapeutic window for PTT. However, both AMB-1 and APPF groups demonstrated significant radiation time-dependent temperature elevation, with APPF exhibiting a bigger temperature increase

 doi:10.20944/preprints202408.0458.v1

(19.5℃) than AMB-1 (16.1℃) at the same concentration (1×10^8 CFU/mL). These results indicated that APPF effectively converted NIR light energy into heat energy. Apart from laser irradiation time, concentration and laser power are two other important factors that influence the photothermal performance of APPF and AMB-1 [30]. As shown in Figure 2b and 2c, APPF exhibited concentration and laser power-dependent temperature elevation. At low concentrations, there was almost no significant temperature increase, but as the concentration increased, the temperature elevation became more pronounced. For example, within 10 min of irradiation, the temperature of the APPF at a concentration of 10×10^7 CFU/mL increased by 19.5℃, while the temperature of the dispersion at a concentration of 1×10^7 CFU/mL increased by only 4.9℃. Likewise, when the concentration was set (1×10^8 CFU/mL), the temperature of APPF increased along with the increase of the laser power. For example, the temperature of APPF increased by 19.5℃ for the group irradiated with a laser power of 1.0 W/cm^2, 37.1℃ for the group irradiated with a laser power of 2.0 W/cm^2, and only 8.2℃ for the group irradiated with a laser power of 0.5 W/cm^2. These results demonstrated that the photothermal behavior of APPF could be precisely controlled by adjusting the irradiation time, laser power, and APPF concentration. Considering that AMB-1 had similar absorption in the near-infrared region and nearly identical photothermal characteristics with APPF, it was reasonably expected that AMB-1 had similar photothermal conversion ability with APPF.

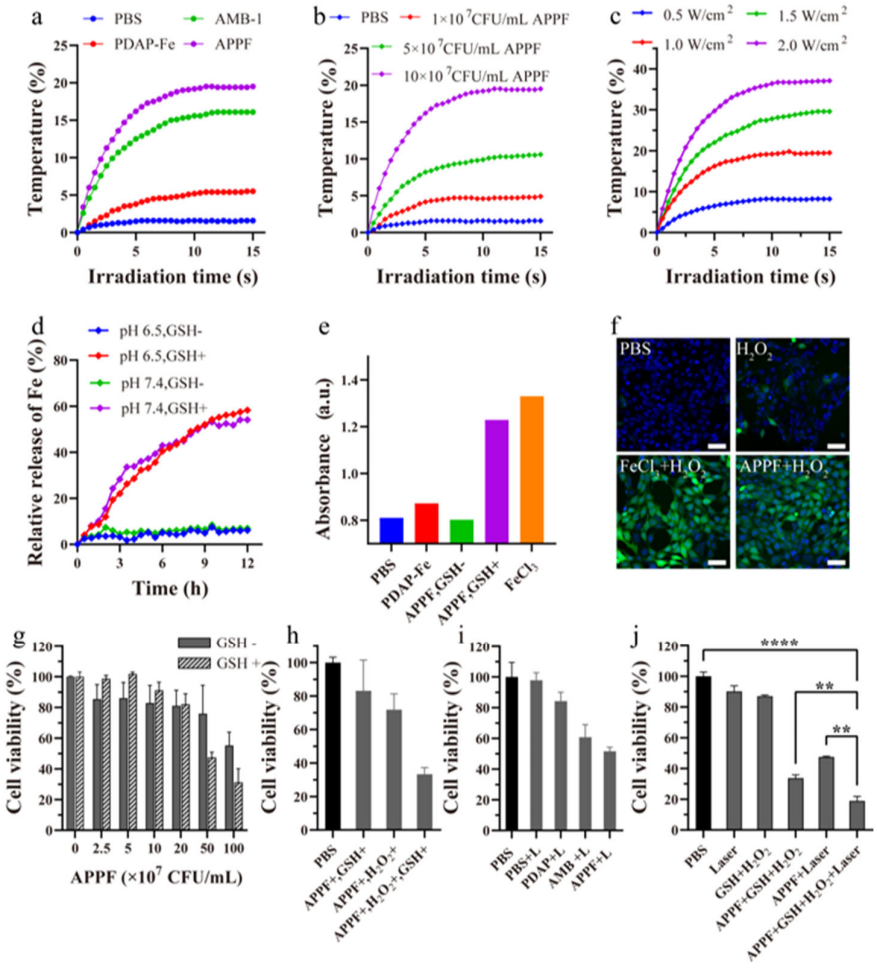

Figure 2. Photothermal performance and Fenton reaction of APPF in vitro**.** (a) Photothermal performance of AMB-1, PDAP-Fe, and APPF under 808 nm laser irradiation; (b) The heating curve of APPF with different concentrations under 808 nm laser irradiation; (c) The heating curve of APPF under 808 nm laser irradiation with different power; (d) The curve of Fe ions released from APPF under different pH values and with or without GSH; (e) UV-vis absorbance of TMB and H_2O_2 solutions incubated with APPF for 20 min at room temperature; (f) Confocal microscope images of

 doi:10.20944/preprints202408.0458.v1

DCFH-DA-stained 4T1 cells 3 hours after treated with H_2O_2, $FeCl_3$+H_2O_2 or APPF+H_2O_2 at pH=6; (g) The cytotoxicity of APPF in 4T1 cells with or without GSH; (h) Anti-tumor effect of APPF-catalyzed Fenton reaction; (i) The viability of 4T1 cells treated with APPF under 808 nm laser irradiation; (j) The in vitro synergistic anti-tumor effect of photothermal therapy and chemodynamic therapy using APPF; 4T1 cells treated with PBS alone was used as a control (100% viability). Unless otherwise specified, the concentration of H_2O_2 was 100×10^{-6} M and the concentration of GSH was 200 μM. * p <0.0001.

The use of Fe^{2+}/Fe^{3+}-catalyzed Fenton reaction to convert H_2O_2 into highly reactive ·OH has been widely studied for cancer therapy [31,32]. To investigate the catalytic performance of APPF, we first examined its ability to release Fe^{2+}. Due to the higher affinity of Fe^{3+} to S than to N, PDAP-Fe in APPF was expected to release Fe^{2+} in the presence of GSH [33]. 200 μM GSH was added to APPF suspension to trigger the reduction of Fe^{3+} and the release of Fe^{2+}. Because Phenanthroline reacts with Fe^{2+} complex, with the products showing a distinct absorption peak at 512 nm [34], we used Phenanthroline to test if any Fe^{2+} was released. The results showed that the loaded Fe ions (~58.3%) were released within 12 hours in the presence of GSH, while almost no Fe^{2+} release was observed in the absence of GSH (Figure 2d). This indicated that GSH effectively triggered the reduction of Fe^{3+} and the release of Fe^{2+}. Importantly, pH had no significant effect on Fe^{2+} release, indicating that APPF specifically responded to GSH to release Fe^{2+}. To monitor if Fenton reaction occurred following Fe^{2+} release, we performed UV-visible light spectroscopy using 3,3,5,5-tetramethylbenzidine (TMB). As shown in Figure 2e, 20 minutes after APPF addition, the TMB/H_2O_2 solution exhibited a measurable increase in absorbance at pH 6.5, similar to the positive control of $FeCl_3$, whereas the absorbance of the PBS group remained unchanged. This result demonstrated that APPF selectively responded to GSH, releasing Fe^{2+} with efficient catalytic activity for Fenton reaction. In tumor cells, high concentration of H_2O_2 exists [35,36], of which Fe^{2+} could catalyze to generate reactive oxygen species (ROS) to activate the apoptotic pathway and promote cell death [37]. To test if this process happened with APPF, we used 2,7-dichlorofluorescein diacetate (DCFH-DA), a commonly used ROS probe [38,39], to detect Fe^{2+}-catalyzed ·OH generation in 4T1 cells. As shown in Figure 2f, cells treated with PBS or H_2O_2 alone exhibited weak fluorescence, while cells treated with APPF and the positive control $FeCl_3$ showed strong green fluorescence. This indicated that APPF effectively catalyzed the generation of ·OH in tumor cells.

The above experiments demonstrated the excellent performance of APPF in performing photothermal and chemodynamic therapy in vitro. Therefore, we further evaluated the anti-tumor effect of APPF at the cellular level. The cytotoxicity of APPF in 4T1 cells was assessed using the Cell Counting Kit-8 (CCK-8) assay. When the concentration of APPF was lower than 2×10^8 CFU/mL, no significant toxicity was observed in the presence or absence of GSH. However, when the concentration of APPF was 5×10^8 CFU/mL, though 4T1 cells with no GSH addition retained a high viability (75.9%), 4T1 cells in the presence of GSH exhibited a significantly low viability (47.5%), possibly due to the release of Fe^{2+} triggered by GSH (Figure 2g). This result indicated that APPF were biosafe when the concentration was below 2×10^8 CFU/mL. Next, we evaluated the anti-tumor effect of APPF-mediated Fenton reaction. As shown in Figure 2h, APPF exhibited mild cytotoxicity in the presence of H_2O_2 alone. However, APPF exhibited a significant anti-tumor effect in the presence of both GSH and H_2O_2, at 1×10^8 CFU/mL, the cell viability decreased by more than 70%. Similarly, under 808 nm laser irradiation, the cell viability of 4T1 cells treated with APPF and AMB-1 decreased significantly, with a reduction of 50% and 40%, respectively (Figure 2h-i), indicating excellent photothermal (PTT) effect of APPF in vitro. To study if any synergistic anti-tumor effect exists, we investigated the combined anti-tumor effect of PTT and Fenton reaction-mediated chemodynamic therapy (CDT) using APPF at a concentration of 1×10^8 CFU/mL and a laser power of 1 W/cm^2. As shown in Figure 2j, when 4T1 cells were treated with APPF, laser, and H_2O_2 in the presence of GSH, over 80% of the cells were killed, indicating a significantly higher anti-tumor effect compared to PTT alone (50%) or Fenton reaction alone (70%). These results revealed the synergistic anti-tumor effect of PTT and Fenton reaction using APPF.

 doi:10.20944/preprints202408.0458.v1

3.3. APPF demonstrates good MRI capability

Magnetic resonance imaging (MRI) is a widely used clinical diagnosis technique with high spatial resolution and real-time monitoring [40]. MRI contrast agents are commonly employed to improve the contrast between the pathological and normal areas, so as to accurately distinguish lesion site from normal tissues. To investigate the contrast enhancement of APPF, longitudinal relaxivity r_1 and transverse relaxivity r_2 of APPF were calculated from the linear fitting of $1/T_1$ and $1/T_2$ plot versus metal concentrations (Figure 3a). The values of r_1 and r_2 are estimated to be 4 and 68 mM^{-1} s^{-1}, respectively. More importantly, the ratio of r2 /r1 is calculated to be 17, which indicates that APPF can be used as both T_1 and T_2 MRI contrast agents. As shown in Figure 3b, APPF present excellent positive T_1 and T_2 contrast enhancement. In T_1 contrast enhancement, the brightness of MR images enhances with the increasing of APPF, whereas in T_2 contrast enhancement, the brightness of MR images decreases along with the increase of APPF, indicating a clear dose-dependent color change. Next, we investigated the in vivo MR imaging performance of APPF. 4T1 tumor-bearing mice were intravenously injected with 200 μL of APPF solution. Figure 3c shows both T_1-weighted and T_2-weighted MR images taken before and after injection. Clearly, with the increase of time, T_1-weighted MR images displayed an increase in brightness, gradually lighting the tumor up (Figure 3c above), whereas T_2-weighted MR images showed a decrease in brightness (Figure 3c below), confirming that APPF can both increase the T_1 MRI contrast and decrease the T_2 MRI contrast in animal models. The signal enhancement was quantified to be 1.2 folds 9 hours post-injection for T_1 enhancement, and 3.4 folds for T_2 enhancement at the same hour. The slow increase of signal intensity over time suggested that APPF accumulated in the tumor site. The in vivo enhanced T_1 and T_2 positive signal of APPF makes it a promising MRI contrast agent to facilitate tumor diagnosis and tumor therapy.

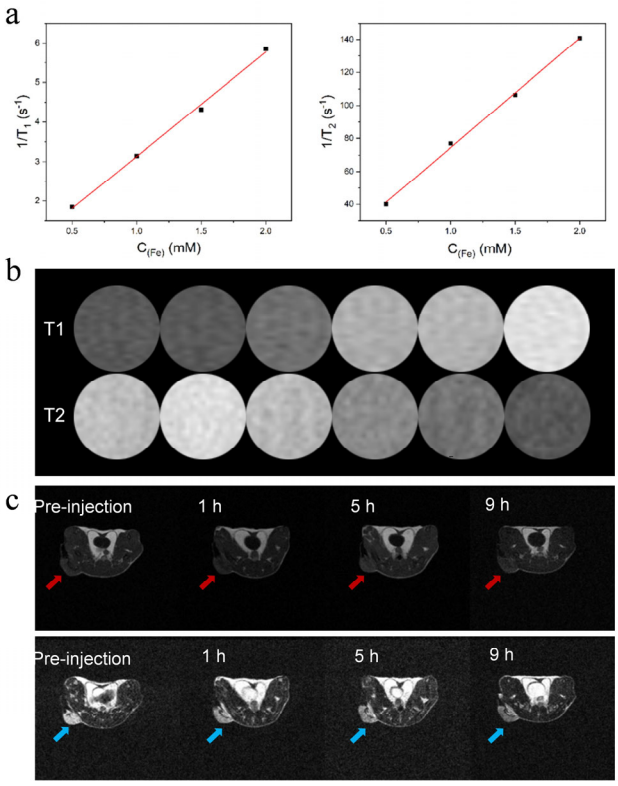

Figure 3. In vitro and in vivo MRI performance of APPF. (a) Plots of $1/T_1$ and $1/T_2$ as a function of total metal (Fe) concentrations. (b) T_1 -weighted MR images (top) and T_2 -weighted MR images (bottom) of APPF at different concentrations. (c) T_1- and T_2-weighted MR images of a 4T1 tumor-bearing mouse before and after intravenous injection of APPF. Tumor regions were highlighted by red and blue arrows.

 doi:10.20944/preprints202408.0458.v1

3.4. Combined photothermal and chemodynamic anti-tumor effect of APPF

After validating the combined anti-tumor effect of APPF at the cellular level and their ability to enhance MR imaging, we evaluated the in vivo anti-tumor effect of APPF. 4T1 tumor-bearing mice were randomly divided into five treatment groups (PBS, PDAP-Fe, APPF, AMB+Laser, APPF+Laser) and treated according to the scheme shown in Figure 4a. Laser irradiation was performed 2 hours after drug injection, and the temperature of the tumor tissue in mice was recorded. As shown in Figure 4b, compared to the PBS injection group (ΔT= 5.8℃), mice treated with AMB+Laser exhibited a significant increase in temperature (ΔT= 13.7℃). Under the same level of laser irradiation, mice injected with APPF showed a greater temperature increase (ΔT= 16.9℃) at the irradiation site. To investigate if APPF had any potential side effects on the tumor-bearing mice, we continuously monitored the body weight of the mice throughout the treatment process. We found that there was no significant change in mouse body weight throughout the entire treatment regimen (Figure 4c), indicating an overall safety of the treatment protocol. More importantly, we continuously monitored the growth of the mice tumors during the treatment process to evaluate the efficacy of different treatment regimens (Figure 4d). In the PBS group, tumor growth was relatively rapid; The PDAP-Fe and APPF groups showed some inhibition of tumor growth, demonstrating the effectiveness of Fenton reaction-mediated cancer therapy. Strong tumor suppression was observed in mice treated with AMB+Laser, indicating the anti-tumor effect of PTT. As expected, the treatment regimen using APPF+Laser exhibited stronger tumor suppression compared to PTT induced by AMB+Laser or CDT induced by PDAP-Fe or APPF alone, which was attributed to the combined PTT and CDT of APPF treatment. At the end of the treatment, differential analysis of tumor volume was performed among the different treatment groups, and the results were consistent with the tumor growth curve, with the APPF+Laser group showing significantly smaller tumor volume than the other treatment groups (Figure 4e, f). To verify the presence of any potential adverse reactions, we studied the postmortem histopathology of the major organs (heart, liver, spleen, lungs, and kidneys). Negligible morphological differences were observed in the organs of each group, further supporting the good biocompatibility of the APPF treatment strategy (Figure 5).

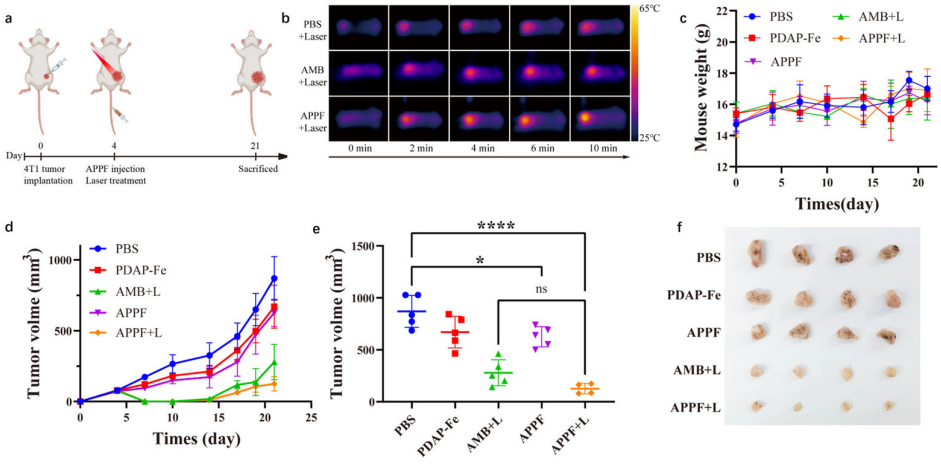

Figure 4. The combined anti-tumor effect of APPF-mediated photothermal therapy and chemodynamic therapy in vivo. (a) Schematic illustration of the treatment schedule; (b) Thermal images of tumor-bearing mice injected intravenously with PBS, AMB-1 or APPF under 808 nm laser irradiation at the indicated time points; (c) Tumor growth curve of mice treated with different protocols; (d) The weight change of the mice in different groups throughout the treatment; (e) Differential analysis of the tumor volume in different treatment groups; (f) Display of the tumor tissue obtained from different treatment groups. The data are shown as mean ± standard deviation. (The number of mice in each group was 4 or 5). * p <0.05, ** p <0.01, *** p <0.001, **** p <0.0001.

 doi:10.20944/preprints202408.0458.v1

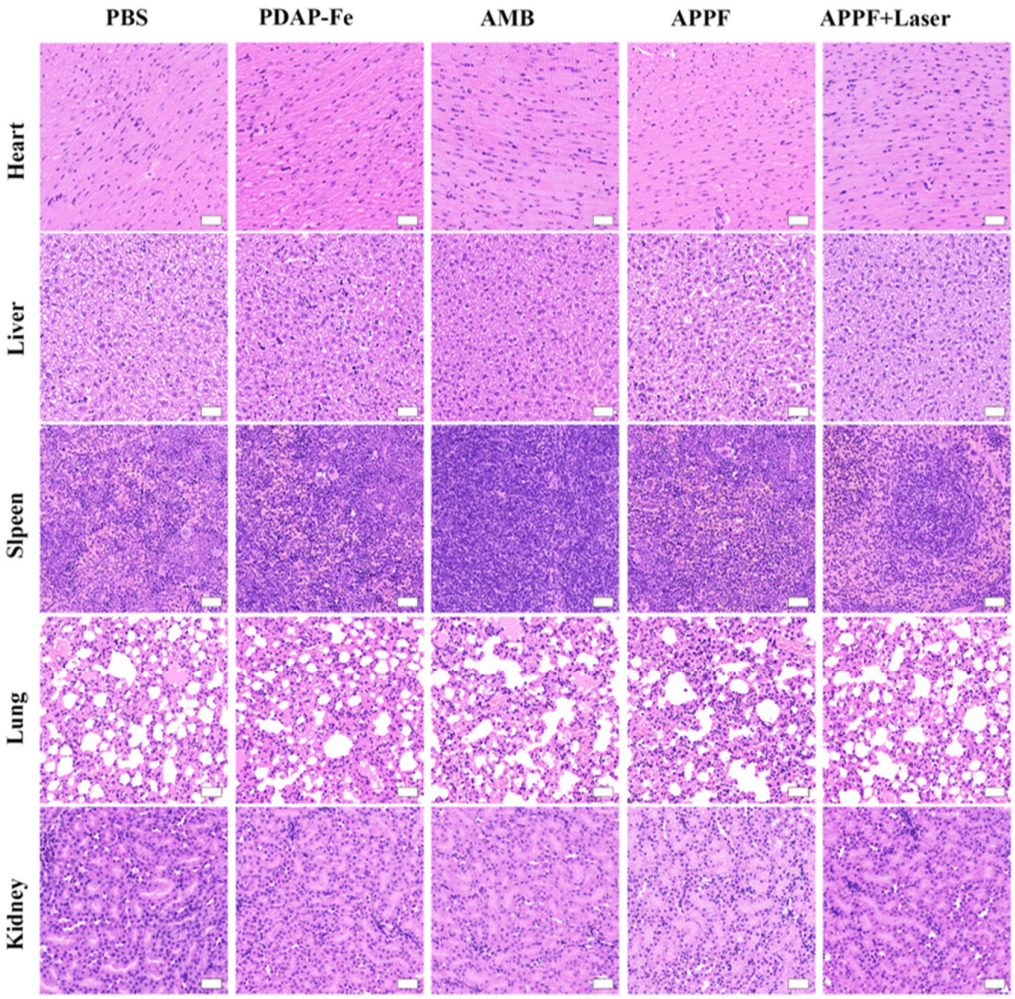

Figure 5. Biosafety assessment of APPF. Post-treatment H&E morphology evaluation of the isolated main organs collected from the mice.

4. Discussion

In summary, we have developed a multifunctional multi-drug delivery platform, APPF, based on the magnetotactic bacterium AMB-1, for MRI-visualized combined photothermal therapy (PTT) and enhanced Fenton reaction-mediated chemodynamic therapy (CDT). By taking advantage of the high affinity of Fe ions to the nitrogen (N) in PDAP, we prepared PDAP-Fe nanoparticles with high loading capacity of Fe ions. The doped Fe^{3+} were reduced by glutathione (GSH) in tumor site, releasing highly active Fe^{2+} to catalyze Fenton reaction, thus the generation of reactive oxygen species (ROS), and the inhibition of tumor growth. Additionally, the magnetite nanoparticles formed inside AMB-1 cells exhibited significant absorption in the near-infrared (NIR) region, enabling efficient conversion of NIR laser energy into heat energy for PTT-based anti-tumor therapy. The PDAP in APPF also contributed to the PTT behavior of APPF. It is noteworthy that the heat generated during PTT accelerated the release of Fe^{2+} from APPF, which enhanced Fenton reaction in the H_2O_2-rich tumor microenvironment for cancer treatment. This work demonstrated the fabrication of a composite multifunctional platform based on the magnetotactic bacterium AMB-1 through simple electrostatic interactions. It further confirmed the synergistic effect of PTT and Fenton reaction-mediated cancer treatment, providing a new alternative for tumor therapy and a new design strategy for the application of magnetotactic bacteria in cancer treatment.

Author Contributions: Conceptualization, Feng Feng, Qilong Li, Xiuyu Wang; Formal analysis, Feng Feng, Li Yao and Xiuyu Wang; Funding acquisition, Xiuyu Wang; Investigation, Feng Feng, Qilong Li and Li Yao; Methodology, Feng Feng, Qilong Li and Xuefei Sun; Supervision, Li Yao and Xiuyu Wang; Validation, Feng Feng, Qilong Li and Xuefei Sun; Visualization, Feng Feng, Qilong Li and Xuefei Sun; Writing – original draft, Feng Feng and Qilong Li; Writing – review & editing, Feng Feng, Qilong Li, Xuefei Sun, Li Yao and Xiuyu Wang. All authors have read and agreed to the published version of the manuscript.

Funding: This work was financially supported by Zhejiang Provincial Natural Science Foundation (209209-J32301ZJ); the National Natural Science Foundation of China (No.209209-N12401ZJ).

Acknowledgments: The authors would like to acknowledge State Key Laboratory of Clean Energy Utilization, Zhejiang University for all the support that they have provided; The authors would also like to acknowledge Institute of Chemistry Chinese Academy of Sciences for all the technical supports they have provided.

Conflicts of Interest: The authors declare no conflicts of interest or personal relationships that could have appeared to influence the work reported in this paper.

References

1. Wahida, A., Buschhorn, L., Fröhling, S. et al. The coming decade in precision oncology: six riddles. Nat Rev Cancer. 2023; 23, 43–54. https://doi.org/10.1038/s41568-022-00529-3
2. Zhang, Z., Xu, X., Du, J. et al. Redox-responsive polymer micelles co-encapsulating immune checkpoint inhibitors and chemotherapeutic agents for glioblastoma therapy. Nat Commun. 2024; 15, 1118. https://doi.org/10.1038/s41467-024-44963-3
3. W.P. Fan, B. Yung, P. Huang, et al. Nanotechnology for Multimodal Synergistic Cancer Therapy. Chem. Rev. 2017; 117 (22), 13566–13638. https://doi.org/10.1021/acs.chemrev.7b00258
4. Timothy A Yap, Eileen E Parkes, Weiyi Peng, et al. Development of Immunotherapy Combination Strategies in Cancer. Cancer Discov. 2021; 11 (6):1368-1397. doi: 10.1158/2159-8290.CD-20-1209
5. Massimo Di Maio, Paolo Chiodini, Vassilis Georgoulias, et al. Meta-Analysis of Single-Agent Chemotherapy Compared with Combination Chemotherapy As Second-Line Treatment of Advanced Non–Small-Cell Lung Cancer. JCO. 2009; 27, 1836-1843. doi:10.1200/JCO.2008.17.5844
6. Datta, S., Grant, D. Crystal structures of drugs: advances in determination, prediction, and engineering. Nat Rev Drug Discov. 2004; 3, 42–57. https://doi.org/10.1038/nrd1280
7. P.P. Yang, Q. Luo, G.B. Qi, et al. Host Materials Transformable in Tumor Microenvironment for Homing Theranostics. Adv. Mater. 2017, 29, 1605869. https://doi.org/10.1002/adma.201605869
8. Wang, Z., Li, W., Jiang, Y. et al. Cholesterol-modified sphingomyelin chimeric lipid bilayer for improved therapeutic delivery. Nat Commun. 2024; 15, 2073. https://doi.org/10.1038/s41467-024-46331-7
9. Y.H. Tsou, X.Q. Zhang, H. Zhu, et al. Drug Delivery to the Brain across the Blood–Brain Barrier Using Nanomaterials. Small. 2017; 13 (43): 1701921. https://doi.org/10.1002/smll.201701921
10. Zanganeh, S., Hutter, G., Spitler, R. et al. Iron oxide nanoparticles inhibit tumour growth by inducing pro-inflammatory macrophage polarization in tumour tissues. Nature Nanotech. 2016; 11, 986–994. https://doi.org/10.1038/nnano.2016.168
11. C.S. Wang, Y.J. Yu, M. Irfan, et al. Rational Design of DNA Framework-Based Hybrid Nanomaterials for Anticancer Drug Delivery. Small. 2020; 44 (16): 2002578. https://doi.org/10.1002/smll.202002578
12. Cheung, A., Zhang, D., Koshy, S. et al. Scaffolds that mimic antigen-presenting cells enable ex vivo expansion of primary T cells. Nat Biotechnol. 2018; 36, 160–169. https://doi.org/10.1038/nbt.4047
13. Zhai, Y., Wang, J., Lang, T. et al. T lymphocyte membrane-decorated epigenetic nanoinducer of interferons for cancer immunotherapy. Nat. Nanotechnol. 2021; 16, 1271–1280. https://doi.org/10.1038/s41565-021-00972-7
14. Jingchao Li, Dong Cui, Jiaguo Huang, et al. Organic Semiconducting Pro-nanostimulants for Near-Infrared Photoactivatable Cancer Immunotherapy. Angew. Chem. Int. Ed. 2019; 36 (58): 12680-12687. https://doi.org/10.1002/anie.201906288
15. Zecong Xiao, Zhenwei Su, Shisong Han, et al. Dual pH-sensitive nanodrug blocks PD-1 immune checkpoint and uses T cells to deliver NF-κB inhibitor for antitumor immunotherapy. Sci. Adv. 2020; 6, eaay7785.DOI:10.1126/sciadv.aay7785.
16. Wei Zhao, Yongmei Zhao, Qingfu Wang, et al. Remote Light-Responsive Nanocarriers for Controlled Drug Delivery: Advances and Perspectives. Small. 2019; 45 (15):1903060. https://doi.org/10.1002/smll.201903060

 doi:10.20944/preprints202408.0458.v1

17. Wilhelm, S., Tavares, A., Dai, Q. et al. Analysis of nanoparticle delivery to tumours. Nat Rev Mater. 2016; 1, 16014. https://doi.org/10.1038/natrevmats.2016.14
18. Yao Liu, Lili Niu, Nannan Li, et al. Bacterial-Mediated Tumor Therapy: Old Treatment in a New Context. Advanced Science. 2023; 15 (10): 2205641. https://doi.org/10.1002/advs.202205641
19. Felfoul, O., Mohammadi, M., Taherkhani, S. et al. Magneto-aerotactic bacteria deliver drug-containing nanoliposomes to tumour hypoxic regions. Nature Nanotech. 2016; 11, 941–947. https://doi.org/10.1038/nnano.2016.137
20. Damien Faivre, Dirk Schüler. Magnetotactic Bacteria and Magnetosomes. Chem. Rev. 2008; 108 (11): 4875–4898. https://doi.org/10.1021/cr078258w
21. Byung-Wook Park, Jiang Zhuang, Oncay Yasa, et al. Multifunctional Bacteria-Driven Micro-swimmers for Targeted Active Drug Delivery. ACS Nano 2017; 11 (9): 8910–8923. https://doi.org/10.1021/acsnano.7b03207
22. Felfoul, O., Martel, S. Assessment of navigation control strategy for magnetotactic bacteria in microchannel: toward targeting solid tumors. Biomed Microdevices. 2013; 15, 1015–1024. https://doi.org/10.1007/s10544-013-9794-4
23. Pingping Wang, Changyou Chen, Qingmeng Wang, et al. Tumor inhibition via magneto-mechanical oscillation by magnetotactic bacteria under a swing MF. J. Control. Release. 2022; 351, 941-953. https://doi.org/10.1016/j.jconrel.2022.09.059
24. Edouard Alphandéry, Imène Chebbi, François Guyot, et al. Use of bacterial magnetosomes in the magnetic hyperthermia treatment of tumours: A review. International Journal of Hyperthermia. 2013; 29 (8): 801-809. https://doi.org/10.3109/02656736.2013.821527
25. Tuanwei Li, Chunyan Li, Zheng Ruan, et al. Polypeptide-Conjugated Second Near-Infrared Organic Fluorophore for Image-Guided Photothermal Therapy. ACS Nano. 2019; 13, 3691-3702. https://doi.org/10.1021/acsnano.9b00452
26. Jing Bai, Xiaodan Jia, Wenyao Zhen, et al. A Facile Ion-Doping Strategy to Regulate Tumor Microenvironments for Enhanced Multimodal Tumor Theranostics. J. Am. Chem. Soc. 2018; 140 (1): 106–109. https://doi.org/10.1021/jacs.7b11114
27. Jingkun Li, Shraboni Ghoshal, Wentao Liang et al. Structural and mechanistic basis for the high activity of Fe–N–C catalysts toward oxygen reduction. Energy Environ. Sci. 2016; 9, 2418-2432. https://doi.org/10.1039/C6EE01160H
28. Lian-Hua Fu, Chao Qi, Yan-Ru Hu, et al. Glucose Oxidase-Instructed Multimodal Synergistic Cancer Therapy. Adv. Mater. 2019, 31, 1808325. https://doi.org/10.1002/adma.201808325
29. Qilong Li, Haitao Chen, Xueyan Feng, et al. Nanoparticle-Regulated Semiartificial Magnetotactic Bacteria with Tunable Magnetic Moment and Magnetic Sensitivity. Small. 2019; 15 (15): 1900427. https://doi.org/10.1002/smll.201900427.
30. Yun Chen, Peiying He, Deblin Jana, et al. Glutathione-Depleting Organic Metal Adjuvants for Effective NIR-II Photothermal Immunotherapy. Adv. Mater. 2022; 34, 2201706. https://doi.org/10.1002/adma.202201706
31. Zhongmin Tang, Huilin Zhang, Yanyan Liu, et al. Antiferromagnetic Pyrite as the Tumor Microenvironment-Mediated Nanoplatform for Self-Enhanced Tumor Imaging and Therapy. Adv. Mater. 2017; 29, 1701683. https://doi.org/10.1002/adma.201701683
32. Ting He, Yanyan Yuan, Chao Jiang, et al. Light-Triggered Transformable Ferrous Ion Delivery System for Photothermal Primed Chemodynamic Therapy. Angew. Chem. Int. Ed. 2021; 60 (11): 6047-6054. https://doi.org/10.1002/anie.202015379
33. Jin Cao, Bin Qiao, Yuanli Luo, et al. A multimodal imaging-guided nanoreactor for cooperative combination of tumor starvation and multiple mechanism-enhanced mild temperature phototherapy. Biomater. Sci. 2020; 8 (23): 6561-6578. https://doi.org/10.1039/D0BM01350A
34. Subrata Kumar Dinda, Sirilata Polepallia and Chebrolu Pulla Rao. Binding of Fe(ii)-complex of phenanthroline appended glycoconjugate with DNA, plasmid and an agglutinin protein. New J. Chem. 2020; 44 (27): 11727-11738. https://doi.org/10.1039/D0NJ01524E
35. Zhongmin Tang, Yanyan Liu, Mingyuan He, et al. Chemodynamic Therapy: Tumour Microenvironment-Mediated Fenton and Fenton-like Reactions. Angew. Chem. Int. Ed. 2019; 58 (4): 946-956. https://doi.org/10.1002/anie.201805664

 doi:10.20944/preprints202408.0458.v1

36. Jing Bai, Xiaodan Jia, Wenyao Zhen, et al. A Facile Ion-Doping Strategy To Regulate Tumor Microenvironments for Enhanced Multimodal Tumor Theranostics. J. Am. Chem. Soc. 2018; 140 (1): 106-109. https://doi.org/10.1021/jacs.7b11114
37. Fantian Zeng, Sureya Nijiati, Longguang Tang, et al. Ferroptosis Detection: From Approaches to Applications. Angew. Chem. Int. Ed. 2023; 62 (35): e202300379. https://doi.org/10.1002/anie.202300379
38. Hao Cai, Ping Tan, Xiaoting Chen, et al. Stimuli-Sensitive Linear–Dendritic Block Copolymer–Drug Prodrug as a Nanoplatform for Tumor Combination Therapy. Adv. Mater. 2022; 34 (8): 2108049. https://doi.org/10.1002/adma.202108049
39. Hong-Bo Cheng, Hao Dai, Xiaoqiong Tan, et al. A Facile, Protein-Derived Supramolecular Theranostic Strategy for Multimodal-Imaging-Guided Photodynamic and Photothermal Immunotherapy In Vivo. Adv. Mater. 2022, 34 (11): 2109111. https://doi.org/10.1002/adma.202109111
40. Wenlong Xu, Krishna Kattel, Ja Young Park, et al. Paramagnetic nanoparticle T1 and T2MRI contrast agents. Phys.Chem. Chem. Phys. 2012, 14, 12687−12700. https://doi.org/10.1039/C2CP41357D